PCCP

PAPER

View Article Online
View Journal | View Issue

Cite this: *Phys. Chem. Chem. Phys.*, 2022, **24**, 22792

3D relaxation-assisted separation of wideline solid-state NMR patterns for achieving site resolution†‡

Adam R. Altenhof,[ab] Michael J. Jaroszewicz,[c] Lucio Frydman *[bc] and Robert W. Schurko *[ab]

Received 23rd February 2022,
Accepted 10th August 2022

DOI: 10.1039/d2cp00910b

rsc.li/pccp

There are currently no methods for the acquisition of ultra-wideline (UW) solid-state NMR spectra under static conditions that enable reliable separation and resolution of overlapping powder patterns arising from magnetically distinct nuclei. This stands in contrast to the variety of techniques available for spin-1/2 or half-integer quadrupolar nuclei with narrow central transition patterns under magic-angle spinning (MAS). Resolution of overlapping signals is routinely achieved in MRI and solution-state NMR by exploiting relaxation differences between nonequivalent sites. Preliminary studies of relaxation assisted separation (RAS) for separating overlapping UWNMR patterns using pseudo-inverse Laplace Transforms have reported two-dimensional spectra featuring relaxation rates correlated to NMR interaction frequencies. However, RAS methods are inherently sensitive to experimental noise, and require that relaxation rates associated with overlapped patterns be significantly different from one another. Herein, principal component analysis (PCA) denoising is implemented to increase the signal-to-noise ratios of the relaxation datasets and RAS routines are stabilized with truncated singular value decomposition (TSVD) and elastic net (EN) regularization to resolve overlapped patterns with a larger tolerance for differences in relaxation rates. We extend these methods for improved pattern resolution by utilizing 3D frequency-R_1–R_2 correlation spectra. Synthetic and experimental datasets, including ^{35}Cl (I = 3/2), ^{2}H (I = 1), and ^{14}N (I = 1) NMR of organic and biological compounds, are explored with both regularized 2D RAS and 3D RAS; comparison of these data reveal improved resolution in the latter case. These methods have great potential for separating overlapping powder patterns under both static and MAS conditions.

1. Introduction

High-resolution techniques are important for separation of overlapping patterns arising from chemically and magnetically nonequivalent sites in solid state NMR (SSNMR) spectra, leading to site-specific resolution and unambiguous spectral assignments. For spin-1/2 nuclei, this includes techniques like phase-adjusted spinning sidebands,[1] magic-angle hopping,[2] and magic-angle turning.[3] For quadrupolar NMR, techniques like multiple-quantum magic-angle spinning (MQMAS),[4,5] satellite-transition MAS (STMAS),[6] dynamic angle spinning (DAS),[7] and double rotation (DOR)[8] are limited to resolving central transition (CT) patterns of half-integer spin quadrupolar nuclei with relatively narrow pattern breadths, of which only a handful (*e.g.*, ^{11}B, ^{17}O, ^{23}Na, ^{27}Al) are routinely investigated. More recently, there have been additional proposals for resolving wideline quadrupolar NMR patterns under MAS conditions;[9–12] while extremely useful, these techniques are limited in their application to ultrawide (UW) NMR spectra with overlapping patterns, due to factors such as limited MQ or ST coherence generation, complicated spinning-sideband manifolds, and/or challenges in precise magic angle settings.[13] Furthermore, few methods are helpful under static (*i.e.*, no MAS) conditions at the present time. Finally, in the case of integer spin NMR where MQMAS experiments are not necessary, high-resolution spectra are difficult to obtain due to the need for extremely precise and stable magic angle settings.[14–16]

An alternative possibility for separating and resolving overlapping magnetic resonance powder patterns is by relying on

---

[a] *Department of Chemistry and Biochemistry, Florida State University, Tallahassee, FL 32306, USA. E-mail: rschurko@fsu.edu; Tel: +1 (850)-645-8614*
[b] *National High Magnetic Field Laboratory, 1800 East Paul Dirac Drive, Tallahassee, FL 32310, USA*
[c] *Department of Chemical and Biological Physics, Weizmann Institute of Science, Rehovot, 7610001, Israel. E-mail: lucio.frydman@weizmann.ac.il*

† All RAS routines are written in MATLAB and are available at **https://github.com/rschurko/RAS**.

‡ Electronic supplementary information (ESI) available: Additional experimental details, experiments, and simulations. See DOI: **https://doi.org/10.1039/d2cp00910b**

different site-specific magnetic resonance properties – for instance, distinct spin relaxation, diffusion and/or dynamical behaviours. The spin evolution defined by these properties is usually given by a basis set of time-dependent exponential functions; hence, subjecting the resulting NMR signals to an inverse Laplace transform (ILT)[17–19] could serve to resolve the individual signals with these distinct properties. This is routinely implemented in low-field NMR and in MRI, where diffusion and relaxation are prime contrast mechanisms;[20–22] however, their routine use in SSNMR is rarer. Lupulescu *et al.* demonstrated that relaxation assisted separation (RAS) could resolve relatively narrow, overlapping CT powder patterns of half-integer quadrupolar nuclei, using a pseudo-ILT with a non-negative least-squares (NNLS) fitting of the relaxation data.[23] Iijima and Shimizu implemented RAS for static ^{2}H NMR,[24] while Boutis and Kausik used it for separating patterns influenced by chemical shift anisotropy (CSA).[25]

We have extended RAS methods for resolving overlapped UW patterns,[26] including those exceeding 250 kHz in breadth due to large anisotropic NMR interactions,[27] using stabilized solutions of the NNLS with Tikhonov regularization (Non-Negative Tikhonov Fitting – NNTF). RAS measurements based on T_1 and T_2^{eff} (*i.e.*, effective T_2) were used to resolve patterns of both half-integer and integer-spin quadrupolar nuclei, as well as spin-1/2 patterns influenced by large CSAs.[26] These precedents could further benefit from the application of WURST[28,29] pulses (for direct excitation)[30] or broadband adiabatic inversion-cross polarization (BRAIN-CP) (for CP-enhanced excitation),[31] combined with measurements of T_1 and T_2 (or T_2^{eff}) relaxation time constants using inversion recovery (IR)[32] and CPMG[33,34] sequences, respectively.[35] In particular, all of these sequences are relatively simple, utilize low RF powers, and can be applied to a wide array of spin-1/2 and quadrupolar nuclei.[27,36,37]

All RAS approaches involve an inversion of the NMR relaxation data, transforming it from the time domain to the relaxation-rate domain. Ill-posed inversion problems of this type are inherently sensitive to experimental noise, and the resulting solutions can be quite unstable.[38] Previous RAS work implemented regularization procedures by incorporating an additional l_2-norm constraint in the NNLS regression,[39,40] truncated singular value decompositions (TSVD),[38,41–43] l_1-norm constraints,[44–46] and elastic net (EN) regularizations;[43,47] the use of neural networks[48] and principal component analyses (PCA) have also improved the robustness of these relaxation measurements.[49,50] Previous work also demonstrated the resolution improvement capabilities of using T_1–T_2 correlations to obtain higher-dimensional relaxation spectra.[42,44,51,52]

This study describes the potential of using improved regularized methods for resolving overlapping SSNMR powder patterns. To this end, protocols were developed to acquire $R_1(T_1^{-1})$- and $R_2(T_2^{-1})$-encoded NMR datasets using WCPMG-IR, BRAIN-CP-IR, and QCPMG-IR pulse sequences.[35] RAS processing of these data employed custom-written routines stabilized with TSVD and EN regularization, which substantially reduce both the computational requirements and sensitivity to artifacts, as well as denoising by PCA. An improved pattern resolution can be realised by encoding both R_1 and R_2 domains, as 3D RAS datasets separating powder patterns along the R_1 and R_2 axes can yield separations that are not achievable from 2D datasets. Experimental applications to the resolution of ^{2}H ($I = 1$), ^{35}Cl ($I = 3/2$) and ^{14}N ($I = 1$) UWNMR datasets are discussed.

2. Theory

2.1 Multidimensional inverse Laplace transforms with EN and TSVD regularization

Although the challenges of and solutions for multidimensional ILT of NMR and MRI relaxation datasets have been described in detail,[38,41,51,53] a summary of the inversion methods used in the current work are explained herein for clarity. 2D or 3D structures defined over a continuous domain are capitalized (*e.g.*, F); their discrete analogues are capitalized and boldfaced (*e.g.*, $\mathbf{F}$); and any 1D vectors are lowercase and boldface (*e.g.*, $\mathbf{f}$). Quantities spanning domains of $R^{m\times 1}$, $R^{m\times n}$, and $R^{k\times m\times n}$, are 1D vectors, 2D matrices, and 3D arrays, respectively.

The problem considered here is that of a signal giving rise to a broad NMR powder pattern, which is undergoing simultaneous exponential decay due to two independent relaxation mechanisms (*e.g.*, T_1 and T_2). This signal can be modelled as:

$$G(\tau,\tau',t) = \iiint K(R_1,R_2,\tau,\tau')\exp(i\nu t)F(R_1,R_2,\nu)\mathrm{d}R_1\mathrm{d}R_2\mathrm{d}\nu + \varepsilon(\tau,\tau',t) \quad (1)$$

where $G(\tau, \tau', t)$ is the signal viewed as a function of a direct, spectrum-encoding acquisition time t and over two indirect relaxation dimensions τ and τ'; $F(R_1, R_2, \nu)$ is a distribution correlating the powder patterns to their associated relaxation rates; $\varepsilon(\tau, \tau', t)$ describes experimental noise; and K is the kernel that encodes the relaxation behaviours. This is modelled as a product of a kernel that encodes R_1, $K_1(R_1, \tau) = 1 - 2\exp(-R_1\tau)$, with a kernel that encodes R_2, $K_2(R_2, \tau') = \exp(-R_2\tau')$ (*vide infra*). The goal of RAS is to estimate $F(R_1, R_2, \nu)$ from $G(\tau, \tau', t)$. This is a 3D inversion problem that can be reduced to 2D by considering eqn (1) on a frequency-by-frequency basis;[41] *i.e.*, by Fourier transforming the signal over the direct-acquisition time dimension, t, such that $G(\tau,\tau',t) \xrightarrow{\mathrm{FT}(t)} G(\tau,\tau',\nu)$. Considering only a single frequency point, ν_k, the problem then reduces to solving a 2D Fredholm integral of the first kind:[38]

$$G_k(\tau,\tau') = \iint K(R_1,R_2,\tau,\tau')F_k(R_1,R_2)\mathrm{d}R_1\mathrm{d}R_2 + \varepsilon(\tau,\tau') \quad (2)$$

This 2D inversion problem is evaluated numerically with a non-negative least-squares (NNLS) regression, which is reduced to a 1D inversion problem by

$$\mathbf{f}_k^{\mathrm{g}} = \min_{\mathbf{f}\geq 0}\left(\|\mathbf{K}\cdot\mathbf{f}_k - \mathbf{s}_k\|_2^{\,2}\right) \quad (3)$$

where discrete matrix representations of $F_k(R_1, R_2)$ and $G_k(\tau, \tau')$ have been vectorized by rearranging and stacking their columns as $\mathbf{f}_k^{\mathrm{g}} \in \mathbb{R}^{(n_1\cdot n_2)\times 1}$ and $\mathbf{s}_k \in \mathbb{R}^{(m_1\cdot m_2)\times 1}$, respectively, and the discrete kernel $\mathbf{K} = \mathbf{K}_1 \otimes \mathbf{K}_2$ with $\mathbf{K} \in \mathbb{R}^{(m_1 \cdot m_2)\times(n_1 \cdot n_2)}$. The label 'g' differentiates the signal $\mathbf{f}^{\mathrm{g}}$ that minimizes the norm from $\mathbf{f}$ in the regression. n_1 and n_2 refer to the number of rates used to model R_1 and R_2 relaxation, respectively, and m_1 and m_2 are the number of experimental time increments used to encode R_1 (τ increments) and R_2 (τ' increments; also, the number of CPMG spin echoes) relaxation rates, respectively. A non-negativity constraint is imposed since the experimental rates describing relaxation are strictly non-negative. Any constraints enforced in the NNLS in general are referred to as regularization (*vide infra*). In general, $\|\mathbf{x}\|_2$ and $\|\mathbf{x}\|_1$ denote the l_2 and l_1 Euclidean norms of $\mathbf{x}$, respectively.

In principle, the resultant $\mathbf{f}^{\mathrm{g}}$ that minimizes the norm in eqn (3) can be transformed back into a matrix for every k, thereby forming a 3D dataset as $\mathbf{F}^{\mathrm{g}} \in \mathbb{R}^{k\times n_1\times n_2}$. Solutions to eqn (3), however, are extremely sensitive to the experimental noise; such problems are classified as ill-posed,[54] and require additional regularization constraints to help stabilize their solutions. Elastic-net (EN) is one form of regularization that we have adopted, and refers to the linear combination of additional l_2 and l_1 norm constraints.[35,47] The additional l_2 norm serves to minimize the condition number of the kernel by penalizing its small non-zero singular values, which attenuates the amplitude of the experimental noise in the NNLS fit. The l_1 norm imposes a sparsity constraint that can force some solutions to zero, which is often useful for multi-component relaxation or distributions of relaxation rates.[45,47] EN regularization introduces these norms into eqn (3):

$$\mathbf{f}_k^{\mathrm{g}} = \min_{\mathbf{f}\geq 0}\left(\|\mathbf{K}\cdot\mathbf{f}_k - \mathbf{s}_k\|_2^2 + \alpha\|\mathbf{f}_k\|_2^2 + \lambda\|\mathbf{f}_k\|_1\right) \tag{4}$$

where α and λ are called the regularization parameters, which are weighting factors for the l_2 and l_1 norm constraints, respectively. The l_2 norm constraint is implemented here using Tikhonov regularization,[26,39,40,54] such that

$$\mathbf{f}_k^{\mathrm{g}} = \min_{\mathbf{f}\geq 0}\left(\left\|\begin{pmatrix}\mathbf{K}\\ \alpha\mathbf{L}\end{pmatrix}\mathbf{f}_k - \begin{pmatrix}s_k\\ 0\end{pmatrix}\right\|_2^2 + \|\lambda\mathbf{f}_k\|_1\right) \tag{5}$$

where $\mathbf{L} \in \mathbb{R}^{(n_1 \cdot n_2 - 2)\times(n_1 \cdot n_2)}$ is the discrete, second-order derivative operator necessary for inversion.[26,43,54,55] In this work, the NNLS regression including the l_1 constraint is evaluated directly in eqn (5) using the novel interior point method developed by Boyd *et al.*[45] The optimal λ for the l_1 norm constraint can be determined with a characteristic S-curve by examining the log of the residual norm as a function of λ (*vide infra*; see Fig. S5, ESI‡).[42,56]

As mentioned, the kernel in eqn (5) is defined as the outer product between the two kernels used to describe R_1 and R_2 relaxation

$$\mathbf{K} = \mathbf{K}_1 \otimes \mathbf{K}_2 \tag{6}$$

where $\mathbf{K}_1 \in \mathbb{R}^{m_1\times n_1}$, $\mathbf{K}_2 \in \mathbb{R}^{m_2\times n_2}$, and $\mathbf{K} \in \mathbb{R}^{(m_1\cdot m_2)\times(n_1\cdot n_2)}$. When many relaxation rates are used to define $\mathbf{K}$, the inversion problem becomes computationally expensive. One approach to overcome the computational cost is to reduce the dimensionality of the problem using truncated singular value decomposition (TSVD).[41,43] The SVD of $\mathbf{K}_i$ (i = 1, 2) can be written as

$$\mathbf{K}_i = \mathbf{U}_i\mathbf{\Sigma}_i\mathbf{V}_i^{\mathrm{T}} \tag{7}$$

where $\mathbf{U}_i \in \mathbb{R}^{m_i\times m_i}$ and $\mathbf{V}_i \in \mathbb{R}^{n_i\times n_i}$ are orthogonal matrices whose columns form the singular vectors of $\mathbf{K}_i$, $\mathbf{\Sigma}_i \in \mathbb{R}^{m_i\times n_i}$ has diagonal non-negative singular value entries σ_r (r = 1, …, m_i) of progressively decreasing magnitude, and the superscript T indicates matrix transposition. To reduce the dimensionality of the kernel, it is projected onto a low-rank subspace using only the first r_i singular values and corresponding singular vectors:

$$\tilde{\mathbf{K}}_i = \mathbf{\Sigma}_i^{r_i}\left(\mathbf{V}_i^{r_i}\right)^{\mathrm{T}} \tag{8}$$

$$\tilde{\mathbf{K}} = \tilde{\mathbf{K}}_1 \otimes \tilde{\mathbf{K}}_2 \tag{9}$$

and the signal is compressed as[41]

$$\tilde{\mathbf{S}}_k = \left(\mathbf{U}_1^{r_1}\right)^{\mathrm{T}}\cdot\mathbf{S}_k\cdot\mathbf{U}_2^{r_2} \tag{10}$$

where $\mathbf{U}_i^{r_i} \in \mathbb{R}^{m_i\times r_i}$, $\mathbf{V}_i^{r_i} \in \mathbb{R}^{n_i\times r_i}$, $\sum_i^{r_i} \in \mathbb{R}^{r_i\times r_i}$, $\tilde{\mathbf{K}} \in \mathbb{R}^{(r_1\cdot r_2)\times(n_1\cdot n_2)}$, $\mathbf{S}_k \in \mathbb{R}^{m_1\times m_2}$, $\tilde{\mathbf{S}}_k \in \mathbb{R}^{r_1\times r_2}$, and r_i is some value less than m_i that is determined with the maximum entropy-based criterion separately for each kernel $\mathbf{K}_i$.[43,57] $\tilde{\mathbf{S}}_k$ is then rearranged into a vector to be used in 1D NNLS as $\tilde{\mathbf{s}}_k \in \mathbb{R}^{(r_1\cdot r_2)\times 1}$. The total dimensionality of the kernel and signal can then be substantially reduced depending on number of singular vectors and values retained, resulting in faster calculations and increased regularization. With these provisions, eqn (5) can be described as the sparse non-negative Tikhonov fitting (sparse NNTF):

$$\mathbf{f}_k^{\mathrm{g}} = \min_{\mathbf{f}\geq 0}\left(\left\|\begin{pmatrix}\tilde{\mathbf{K}}\\ \alpha\mathbf{L}\end{pmatrix}\mathbf{f}_k - \begin{pmatrix}\tilde{\mathbf{s}}_k\\ 0\end{pmatrix}\right\|_2^2 + \lambda\|\mathbf{f}_k\|_1\right) \tag{11}$$

where the total concatenated kernel size is $\mathbb{R}^{(r_1\cdot r_2+n_1\cdot n_2-2)\times(n_1\cdot n_2)}$ and the concatenated signal size is $\mathbb{R}^{(r_1\cdot r_2+n_1\cdot n_2-2)\times 1}$. As mentioned, this way of casting the ILT problem then needs to be evaluated for every frequency point, k (k = 1, 2, 3, …, np) defining the SSNMR powder pattern, the result of which is used to form the 3D dataset $\mathbf{F}^{\mathrm{g}}$.

2.2 Spectral denoising with principal component analysis

A 3D ν–R_1–R_2 correlation experiment, as described above, can be useful for achieving high resolution; however, its performance is sensitive to the signal-to-noise ratio (SNR) – a parameter that directly affects the performance of any NNLS regression. Spectral reconstruction with principal component analysis (PCA) can be implemented to increase overall SNRs.[49,50] PCA fundamentally operates along similar lines of the SVD described in eqn (7), except in this case the matrix of the centered 2D NMR signal $\mathbf{X} = G(\tau, \nu)$ or $G(\tau', \nu)$ is factored with SVD. If $\mathbf{X}$ is the centered matrix of G according to

$$\mathbf{X} = \left(\mathbf{x}_1 - \bar{\mathbf{x}}_1, \ldots \mathbf{x}_p - \bar{\mathbf{x}}_p\right)^{\mathrm{T}} \tag{12}$$

where p is the column index for $\mathbf{X}$, then the SVD of $\mathbf{X}$ is

$$\mathbf{X} = \mathbf{U}\mathbf{\Sigma}\mathbf{V}^{\mathrm{T}} \tag{13}$$

where the columns of $\mathbf{V}$ are the principal directions/axes of $\mathbf{X}$, and the columns of $\mathbf{U}\cdot\mathbf{\Sigma}$ are the corresponding principal components.

Similar to TSVD, only the first b columns are retained from $\mathbf{V}$ and $\mathbf{U}\cdot\mathbf{\Sigma}$, which are a lower variance representation of the data (*i.e.*, a low dimensional subspace or projection). The signal is then reconstructed as

$$\mathbf{Z}_j = \mathbf{U}_j^b \mathbf{\Sigma}_j^b (\mathbf{V}_j^b)^{\mathrm{T}} \tag{14}$$

where $\mathbf{Z}$ has the same dimensions as $\mathbf{X}$ but is now of lower rank, and j indexes the relaxation-delay increment (*i.e.*, τ_j or τ'_j). The 2D NMR signal is thus denoised for every point in the other relaxation dimension. For example, every 2D ν–τ plane of the 3D data is individually denoised for each j ($j = 1, 2, 3, \ldots m_2$) number of echoes using this procedure. It is possible to determine b with a maximum entropy criterion (*vide supra*); however, we have empirically found robust performance with $b = 2$ or 3 throughout this work. It is important to note that PCA denoising is performed during pre-sparse NNTF processing, on the input NMR relaxation data (*i.e.*, before evaluating eqn (11)); in this way the data is denoised without augmented spectral features, and retains its original dimensions.

3. Experimental methods

3.1 Samples

Glycine HCl [Sigma Aldrich], histidine monohydrate HCl [Sigma Aldrich], isoxsuprine HCl [Sigma Aldrich], xylazine HCl [VWR], betaine HCl [Sigma Aldrich], and 1,8-dimethylnapthalene-d_{12} [Cambridge Isotopes] were purchased; all were all used in subsequent NMR experiments without further purification. The identities and purities of the samples were verified through comparisons with previously reported NMR spectra.[58–61] A novel RbCl:CdCl$_2$:Urea cocrystal was prepared mechanochemically *via* ball milling of the dried reagents in the appropriate molar ratios (1 : 1 : 1): rubidium chloride [Sigma Aldrich], cadmium chloride [Sigma Aldrich], and urea [Sigma Aldrich]. This synthesis used a Retsch Mixer Mill 400, 10 mL stainless steel milling jars, and two 7 mm stainless steel ball bearings. All samples were ground into fine powders and packed into 5 mm outer-diameter glass tubes that were sealed with Teflon tape.

3.2 Solid-state NMR spectroscopy

NMR spectra were acquired using a Bruker Avance NEO console and a 14.1 T Magnex/Bruker ($\nu_0(^1\mathrm{H})$ = 600 MHz) wide-bore magnet at resonance frequencies of $\nu_0(^{14}\mathrm{N})$ = 43.348 MHz, $\nu_0(^{35}\mathrm{Cl})$ = 58.792 MHz, and $\nu_0(^2\mathrm{H})$ = 92.104 MHz. A home-built 5 mm double-resonance (HX) probe was used for all experiments. All data were collected under static conditions (*i.e.*, stationary samples). Spectra were acquired with ^{1}H continuous-wave (CW) decoupling using RF fields of 50 kHz. RF pulse powers and chemical-shift reference frequencies were calibrated using the following standards: (i) ^{14}N reference: NH$_4$Cl with δ_{iso} = 0 ppm; (ii) ^{35}Cl reference: NaCl (*s*) with δ_{iso} = 0.0 ppm; and (iii) ^{2}H reference: D$_2$O (*l*) with δ_{iso} = 4.8 ppm.

3.3 Spectral processing

All datasets were processed in MATLAB using custom-written code. NMR data were acquired using pulse sequences that implemented inversion-recovery (IR) – sometimes with the aid of an adiabatic pulse and CPMG refocusing: WCPMG-IR, BRAIN-CP-IR, or QCPMG-IR (Scheme 1).[35,62] During each IR delay increment, τ, NMR signals were acquired with CPMG-windowed acquisitions; the individual spin echoes where then individually Fourier transformed and phase-corrected with an automatic zeroth, first, and second-order phasing routine, resulting in a 3D dataset, $G(\tau, \tau', \nu)$. For 2D RAS processing, the 3D dataset was summed over the rate dimension that is not being analyzed. For example, R_1-RAS was accomplished by summing over the entire R_2 dimension in the 3D dataset, resulting in a 2D $G(\tau, \nu)$ data set. Thirty-two logarithmically sampled τ increments were measured in every experiment. SNRs were calculated as the ratio of maximum spectral intensity to the standard deviation of the baseline noise along the relaxation dimension for a 1D slice of any 2D or 3D dataset presented herein: SNR = $\max(\mathbf{s})/\sigma_{\mathrm{noise}}$.[63,64] Sparse NNTF was calculated in MATLAB using custom code that implements the regularization toolbox by Hansen[55] and the l_1-regularized NNLS routine of Boyd *et al.*[45] All MATLAB code used is available at github.com/rschurko/RAS; simulation input files and pulse programs are available from the authors upon request.

4. Results and discussion

4.1 Overview

WCPMG-IR, BRAIN-CP-IR, or QCPMG-IR pulse sequences (Scheme 1) were used to experimentally acquire 3D ν–τ–τ' datasets.[35] R_1 was encoded *via* IR over a logarithmically incremented delay τ, leading to an exponential recovery of the form $1 - a\exp(-R_1\tau)$, where $a = 2$ for direct excitation, and $a = 1 + \varepsilon$ for CP, where ε is the CP enhancement factor.[35] R_2's were encoded with CPMG sequences over a delay τ' that was linearly incremented *via* the number of CPMG loops, N (where $N = m_2$ in the theory section), leading to an exponential decay of the form $\exp(-R_2\tau')$ (N.B.: R_2 is in fact reflecting the effective T_2, T_2^{eff}, in cases where ^{1}H-S dipolar coupling is present and decoupling is active on the ^{1}H channel; however, herein R_2 is used in every case for simplicity of notation). The result is a 3D data set, but since the τ' increments are obtained as a result of windowed CPMG acquisitions, the experimental time requirements are the same as those of a standard 2D NMR experiment. For both T_1 and T_2, it is also possible that the encoded relaxation behaviour is multiexponential. An example of an experimental 3D ν–τ–τ' dataset is shown in the (Fig. S1, ESI‡).

Herein, we describe the use of BRAIN-CP-IR, WCPMG-IR, and QCPMG-IR experiments to acquire experimental 2D or 3D datasets suitable for RAS. First, the application of 2D RAS is benchmarked on synthetic datasets to systematically demonstrate the outcomes of EN and TSVD regularization methods as well as those of PCA denoising; these methods are then tested with one experimental ^{2}H (I = 1) dataset. Second, 3D RAS is demonstrated with synthetic datasets that outline the processing

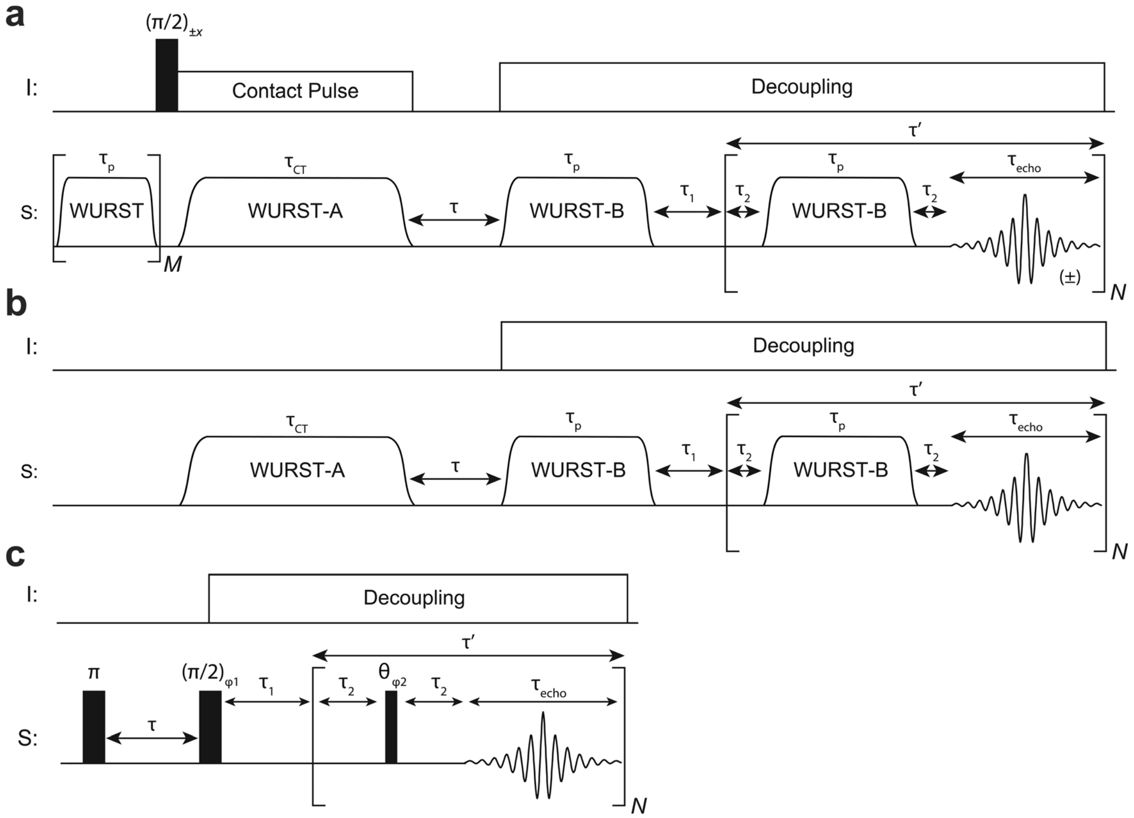

Scheme 1 (a) The BRAIN-CP-IR pulse sequence, (b) the WCPMG-IR pulse sequence, and (c) the QCPMG-IR pulse sequence. The delay time, τ, is logarithmically incremented in every case which encodes R_1 relaxation. τ' represents the R_2 encoding, which is incremented linearly *via* the number of loops, N. In (a) the phase of the ^{1}H excitation pulse controls whether signal is stored as $\pm S_z(t)$ during τ; this can also vary depending on the WURST-A sweep direction. These details have been previously described.[35] In (c) a θ refocusing pulse is used for signal enhancement and φ_1 and φ_2 are incremented with an 8-step phase cycle.[62,65–67]

pipeline and test these same numerical methods. Finally, 3D RAS is demonstrated for several experimental datasets and compared with 2D RAS, including ^{35}Cl (I = 3/2), ^{2}H (I = 1), and ^{14}N (I = 1) NMR examples that show the potential of 3D RAS for separating overlapping powder patterns with clearly resolved features.

4.2 2D RAS

The effects of EN and TSVD regularization were first examined using a 2D implementation of the sparse NNTF inversion described above, as applied to ν–τ or ν–τ' datasets. To this end, a synthetic CPMG dataset of two overlapping powder patterns, with parameters typical of ^{35}Cl in organic hydrochloride (HCl) salts, was used as input (Fig. S2, ESI‡); 100 echoes were simulated across the $\tau'(R_2)$ dimension and 1000 logarithmically spaced rates supplied to the kernel. The size of the kernel was $\mathbf{K} \in \mathbb{R}^{(100)\times(1000)}$ without TSVD and $\tilde{\mathbf{K}} \in \mathbb{R}^{(22)\times(1000)}$ with TSVD, resulting in much faster calculations in the latter case. Fig. 1 (and Fig. S3, ESI‡) shows evaluations of the sparse NNTF for several input signals with distinct SNRs, and for different R_2 rates applied to each powder pattern. In these simulations, α represents the amount of l_2 regularization, which can be determined with a characteristic L-curve;[26,55] the resulting optimal α is often on the order of the standard deviation of the noise and is set as such throughout. λ represents the amount of l_1 regularization, which can vary depending on the amount of noise and/or how close the rates or distributions of rates are to one another. If λ is set too low, then no sparsity is imposed – but if it is too high, then multiple unique rates will appear as just a single rate distribution in the RAS spectrum, thereby hindering pattern separation (Fig. S4, ESI‡). The optimal λ is determined using a S-curve routine in this work (Fig. S5, ESI‡).[42,56]

These simulations show that when the supplied rates are far apart (*e.g.*, $R_{2,\mathrm{A}} = 0.2\ \mathrm{ms}^{-1}$ and $R_{2,\mathrm{B}} = 0.033\ \mathrm{ms}^{-1}$) and the SNR of the input data is high, two distinct rate distributions are observed in the frequency-R_2 contour plot and the 1D R_2 projection, where each corresponds to a distinct powder pattern in the CPMG dataset (Fig. 1a). Solutions in this relatively low-noise regime are stable and provide two distinct rate distributions even as the rates become increasingly similar (Fig. 1b and 1c). As the SNR decreases, two isolated rate distributions can still be identified when the rates are far apart (Fig. 1d), but the distributions start to overlap as the rates get closer (Fig. 1e); however, the sparsity constraint of l_1 regularization still helps to maintain two distinct distributions, as evidenced by the two peaks in the R_2-dimension (even though there is still some degree of overlap). Eventually, if noise is high and rates are closely spaced, two distributions are not identifiable even with

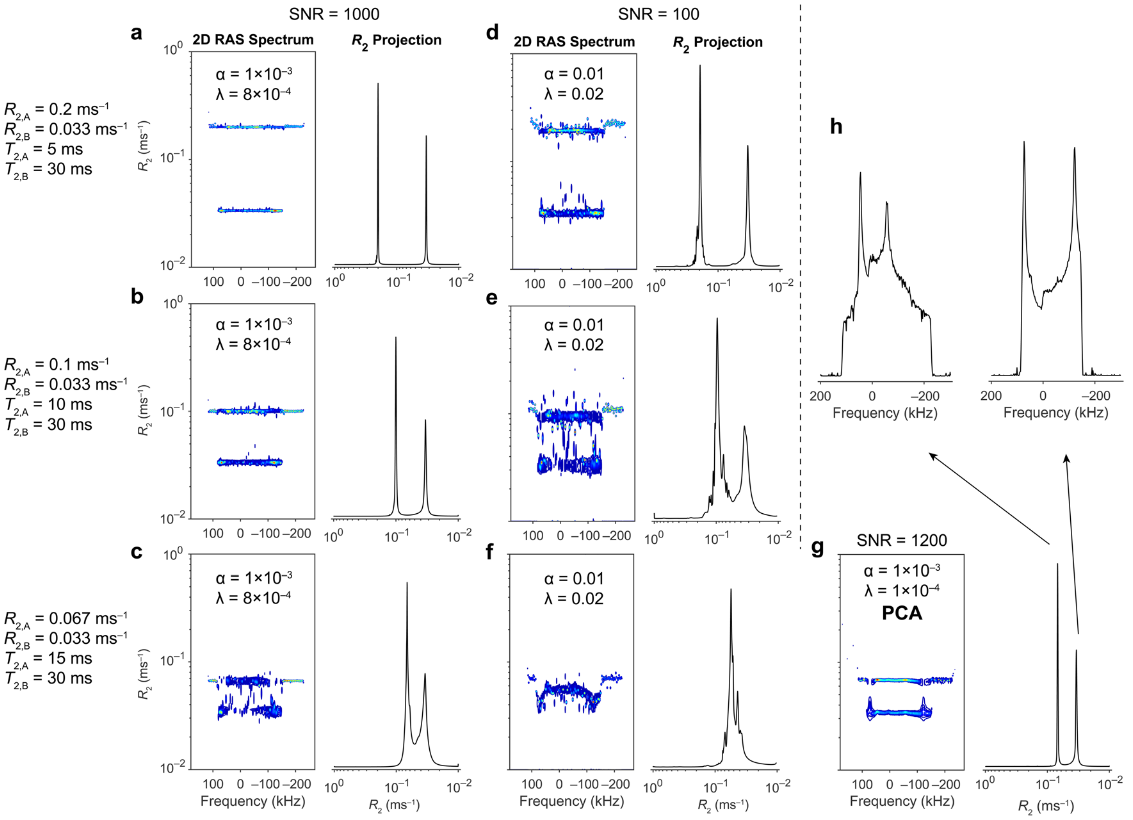

Fig. 1 2D R_2 RAS of simulated nonequivalent CT powder patterns using synthetic CPMG data. The simulated patterns correspond to the case of two magnetically-distinct ^{35}Cl nuclei with EFG tensor parameters of C_Q = 10 and 9.8 MHz and η_Q = 0.6 and 0.1, respectively, at 14.1 T. The first two columns show the 2D RAS ν–R_2 contour spectrum and a projection of the corresponding 1D R_2 dimension for different SNRs, as indicated. Each row has a unique combination of applied rates $R_{2,A}$ ($T_{2,A}{}^{-1}$) and $R_{2,B}$ ($T_{2,B}{}^{-1}$). In every case (a–g) the regularization parameters used for RAS are noted as α for the l_2 norm and λ for the l_1 norm constraint, respectively. (g) The same input signal as (f) is denoised using PCA prior to RAS. (h) Projections of the individual powder patterns from their respective rate distributions in the RAS spectrum from (g).

EN and TSVD regularization (Fig. 1f). This can be problematic, resulting in either long experimental times for improving the SNR, or preventing studies of intrinsically insensitive or chemically dilute nuclei of interest. Reconstructing the input data with

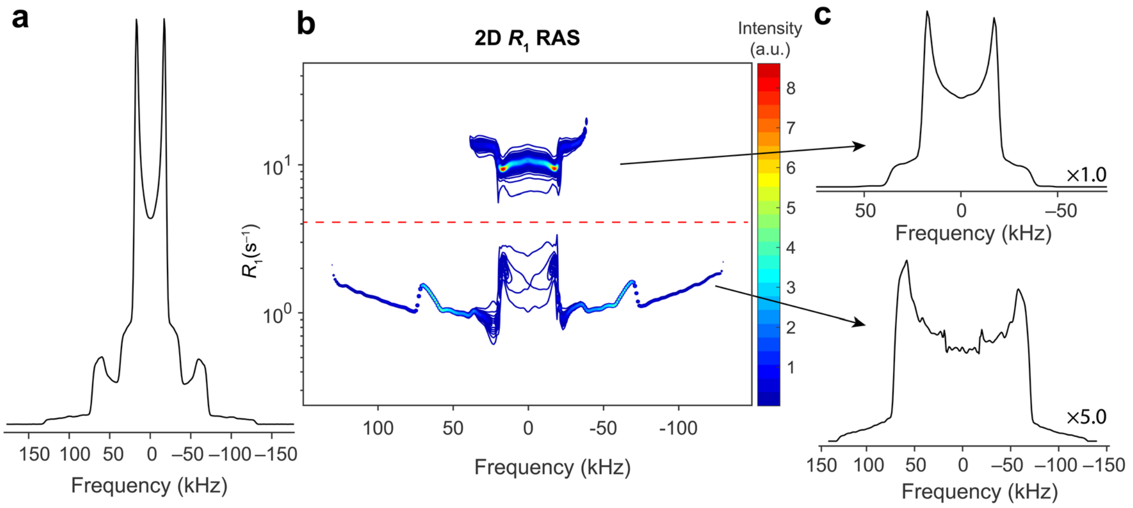

Fig. 2 (a) Experimental 1D ^{2}H NMR of 1,8-dimethylnaphthalene-d_{12}. (b) 2D R_1 RAS of 1,8-dimethylnapthalene-d_{12} with regularization parameters α = 0.015 and λ = 0.02 using R_1 data acquired with QCPMG-IR as input. PCA denoising was not necessary for this dataset. (c) Projections of the powder patterns associated with each rate distribution from above and below the dashed red line from the RAS spectrum. Relative intensities of the patterns are scaled according to the factors on the right.

PCA (eqn (12)–(14)), which effectively discards high-noise (or high-variance) components in the spectral data,[49] can alleviate this problem. This is illustrated in Fig. 1g, which took the input data corresponding to the challenging case above (Fig. 1f), and reconstructed it using just two principal components. PCA improves the SNR of the input relaxation data (*i.e.*, the data pre-processed before sparse NNTF) by approximately a factor of 12, making the solution of the 2D RAS problem much more stable and identifying the correct rate distributions with little overlap and few artifacts. Individual powder patterns can be projected from their respective rate distributions (Fig. 1g), revealing complete separation from one another (Fig. 1h).

2D RAS processing was applied to an experimental ^{2}H NMR dataset for 1,8-dimethylnapthalene-d_{12}, for the purpose of separating the overlapping powder patterns. The 1D NMR spectrum shows two nonequivalent ^{2}H sites associated with methyl and aromatic deuterons (Fig. 2a).[61] A modified QCPMG-IR sequence (Scheme 1) was used to encode R_1's for either site while providing T_2-weighted signal enhancement in this case, where the refocusing pulses use a flip angle of $\theta = 36°$ for signal enhancement.[62,67–71] The 2D R_1 RAS sparse NNTF routine with EN and TSVD regularization results in a 2D spectrum indicating unique R_1 distributions for each deuteron site (Fig. 2b). PCA denoising was not necessary for this dataset. The added regularization constraints permit high-resolution separation of the overlapped powder patterns. These distributions are characteristic of R_1-anisotropy as has been previously observed in ^{2}H SSNMR spectra.[35,72,73] There is a low intensity (*i.e.*, <1% max spectral intensity) rate distribution around 0 Hz for the broad aromatic site, since in this frequency region, the two patterns are the most overlapped in the 1D spectrum and the pattern corresponding to the aromatic site is approximately five

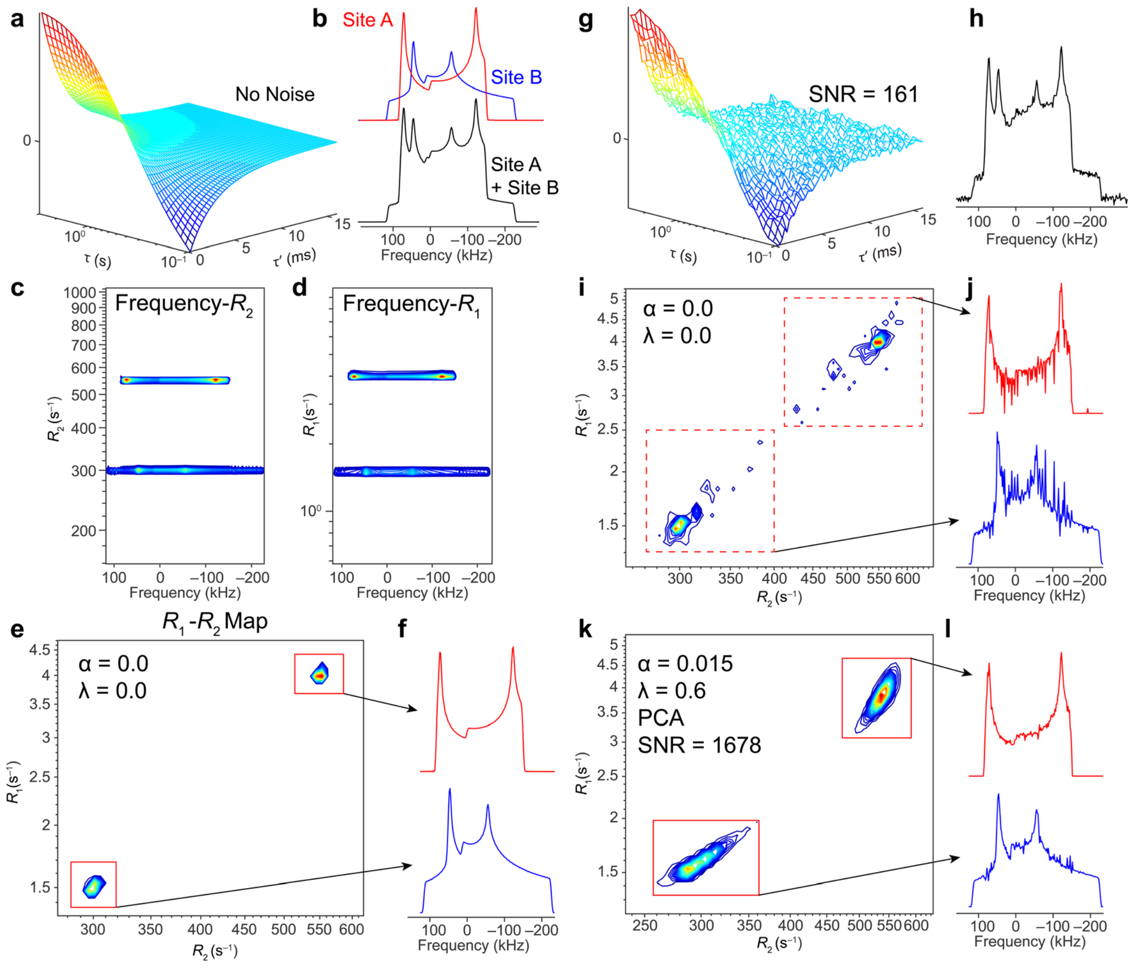

Fig. 3 (a) Synthetic τ–τ' data at a single frequency point ($\mathbf{S}_k$) of two nonequivalent simulated ^{35}Cl NMR patterns that are summed together and used as input for 3D RAS without added noise and (b) 1D frequency representation of the individual sites and their sum. The patterns are simulated with EFG tensor parameters of C_Q = 10 and 9.8 MHz and η_Q = 0.6 and 0.1 for sites A and B, respectively, at 14.1 T. Relaxation time constants are applied for each site with $R_{1,A}$ = 4 s^{-1}, $R_{1,B}$ = 1.5 s^{-1}, $R_{2,A}$ = 550 s^{-1}, and $R_{2,B}$ = 300 s^{-1}. 2D projections after performing 3D RAS on the synthetic 3D dataset of the mixture for the (c) ν–R_2 projection (summed over the R_1 dimension) and the (d) ν–R_1 projection (summed over the R_2 dimension). (e) The R_1–R_2 correlation map obtained by summing over the frequency dimension; no regularization is used as indicated by α = 0.0 and λ = 0.0. (f) Projections of the individual powder patterns associated with each rate distribution. (g) Synthetic τ–τ' data with added noise and (h) a 1D frequency representation of the data. The R_1–R_2 correlation map after 3D RAS (i) without regularization (α = 0.0, λ = 0.0), and (k) with regularization and PCA reconstruction such that the SNR of the input data increases (*i.e.*, the SNR prior to RAS processing). (j and l) Projections of the individual powder patterns associated with the rate distributions in each case.

times less intense than that of the methyl site. Summing over specified rates in the distribution can recover uniform powder patterns corresponding to each site; the rates that are summed over can easily be fine-tuned for optimal separation (*i.e.*, as represented by the dashed red line in Fig. 2b). Projections of the powder patterns from each rate distribution reveal ^{2}H patterns that match well with typical line shapes for ^{2}H methyl and aromatic moieties (Fig. 2c). 2D R_2 RAS in this example was not as useful as R_1-encoding, as both ^{2}H sites have similar, closely overlapping R_2 distributions; however, the R_2 encoding may be useful for 3D RAS for this sample (*vide infra*).

It is important to note that, in general, the rate distributions associated from 2D RAS may not correspond to the ground-truth rate values (*i.e.*, the exact rate distributions, R_1 and/or R_2, that could be measured in the absence of noise): sparse NNTF solutions are sensitive to the experimental noise, which can bias the calculated, inverted rates. Regularization can stabilize the solutions; however, it can also affect the inverted rate distributions – especially the l_1 norm constraint used in EN.[47] In the current work, RAS is used to resolve overlapped patterns; hence, the resulting rates should be interpreted with caution and verified with other methods.[35]

4.3 3D RAS

Synthetic datasets for 3D RAS used simulated spectra based on two overlapping static CT patterns corresponding to two non-equivalent ^{35}Cl sites though in principle, the shape of the frequency pattern could be anything (*e.g.*, CSA patterns, Pake doublets, spinning sideband manifolds, disordered distributions, *etc.*). The two sites (A and B) were simulated with EFG tensor parameters of C_Q = 10 and 9.8 MHz and η_Q = 0.6 and 0.1, respectively, at a 14.1 T field and relaxation time constants are applied for each site with $R_{1,A} = 4\ \mathrm{s}^{-1}$, $R_{1,B} = 1.5\ \mathrm{s}^{-1}$, $R_{2,A} = 550\ \mathrm{s}^{-1}$, and $R_{2,B} = 300\ \mathrm{s}^{-1}$. IR behavior is modelled with 32 logarithmically-spaced τ increments, and transverse decays are modelled with 64 linearly-spaced CPMG echoes (Fig. 3a and b). R_1 and R_2 kernels were sampled with 200 rates each, resulting in a kernel size of $\mathbf{K} \in \mathbb{R}^{(2048)\times(40000)}$ without TSVD and $\tilde{\mathbf{K}} \in \mathbb{R}^{(78)\times(40000)}$ with TSVD, again offering a substantial reduction in computational cost. Eqn (11) was evaluated for the $\mathbf{S}_k$ dataset after rearranging it into a vector for sparse NNTF input as $\mathbf{S}_k \xrightarrow{\text{TSVD}} \tilde{\mathbf{S}}_k \xrightarrow{\text{rearrange}} \tilde{\mathbf{s}}_k$ for every frequency point, initially without l_1 and/or l_2 regularization in this example. The output is therefore a vector containing the joint R_1 and R_2 rate distributions that can be rearranged into a matrix $\mathbf{f}_k^g \xrightarrow{\text{rearrange}} \mathbf{F}_k^g$ for every frequency point, thereby yielding a multidimensional array describing R_1, R_2, and ν. As this can be difficult to visualize and interpret, it may be useful to instead examine the 2D ν–R_2 (Fig. 3c) or ν–R_1 plots (Fig. 3d), which are generated by summing over all the rates in the opposite rate dimension. Sometimes, it is also beneficial to examine the 2D R_1–R_2 correlation map by summing over all frequency points (Fig. 3e). 2D RAS processing of the noiseless,

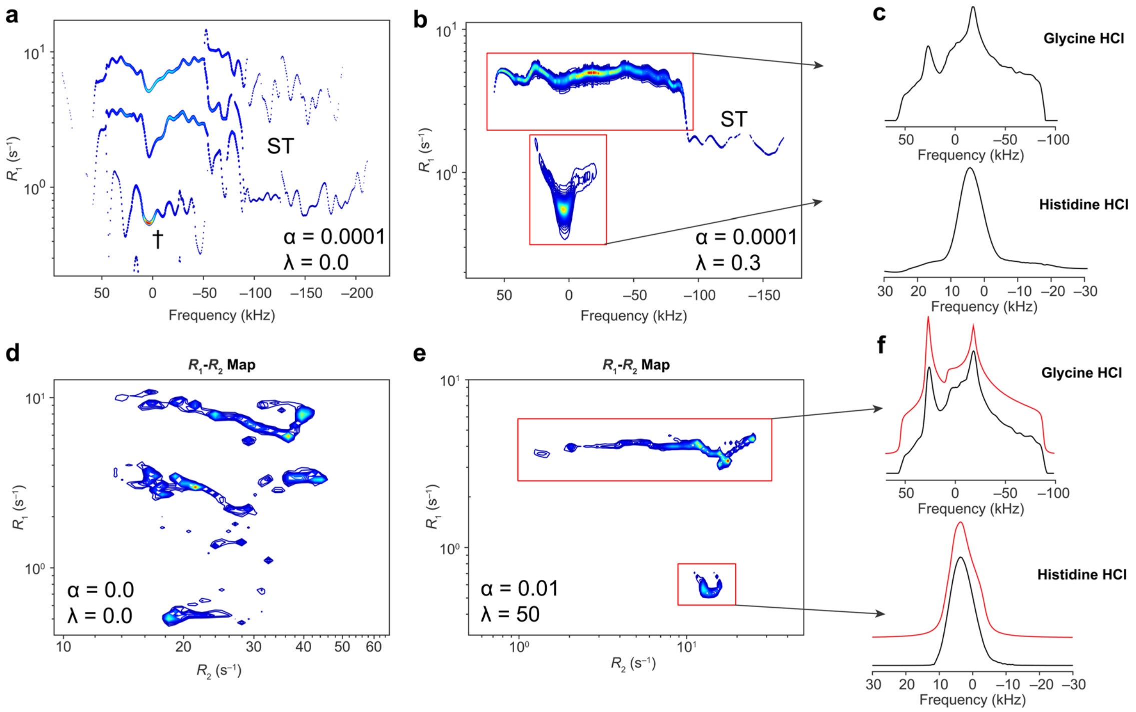

Fig. 4 Experimental ^{35}Cl 2D R_1 RAS NMR spectrum of a glycine HCl : histidine HCl 3 : 1 w/w mixture with regularization parameters (a) α = 0.0001 and λ = 0.0 and (b) α = 0.0001 and λ = 0.3. PCA denoising was not necessary for this dataset. In (a) the histidine pattern is indicated with †, and the ST signal is denoted below *ca.* 80 kHz. (c) Projections of the powder patterns from each of the highlighted rate distributions in (b). R_1–R_2 correlation obtained from 3D RAS with sparse NNTF (d) without EN regularization and (e) with regularization. (f) Projections of the powder patterns from each rate distribution in (e) with ideal ^{35}Cl NMR simulations of each pattern in red.

two-site synthetic dataset yields a R_1–R_2 correlation map showing just two high-resolution peaks, as expected. Each peak appears at rates that match perfectly with the simulated rates, as do the projections of both powder patterns extracted from each of the unique rate distributions (Fig. 3f).

The same dataset is presented in Fig. 3g and h, except with the addition of Gaussian noise. The R_1–R_2 correlation map arising after performing 3D RAS without any regularization (Fig. 3i) shows many spurious artifacts, and a low-resolution "smear" of the signal between the two expected (R_1, R_2) solutions. This complicates the identification of the two components from projections, and the retrieval of clean powder patterns (Fig. 3k). PCA denoising based on two principal components improves the SNR of the input relaxation signal by approximately an order of magnitude, greatly improving the performance of the sparse NNTF. The resulting R_1–R_2 correlation maps then show two distinct components corresponding to each powder pattern (Fig. 3j) that can be projected separately with only minor distortions originating from the noise (Fig. 3l).

Using these numerical methods, the experimental 3D ν–R_1–R_2 ^{35}Cl NMR dataset of a glycine HCl : histidine HCl 3 : 1 w/w mixture (Fig. S1, ESI‡) was processed using both 2D and 3D RAS. The benefits of regularization from l_1 and l_2 penalties are first compared using a 2D R_1-RAS example. 2D R_1-RAS is initially used with only TSVD and l_2 Tikhonov regularization (Fig. 4a), similar to the NNTF method previously reported by our research group.[26] An intense narrow signal is identifiable around +5 kHz and below $R_1 = 1$ s^{-1}, which is likely associated with histidine HCl (denoted by †); however, there is still a substantial amount of broad signal (*i.e.*, above 10 kHz and below −10 kHz) around the same rate distribution that likely corresponds to glycine HCl. Above $R_1 = 1$ s^{-1}, the broad glycine HCl powder pattern appears to span two general rate distributions with several artifacts, which agrees with the observation that the T_1(^{35}Cl) for glycine HCl is described by a biexponential decay.[35] Additionally, there is signal intensity outside of the bandwidth of the CT powder pattern of glycine HCl that appears at multiple rates below *ca.* −80 kHz, which is likely ST signal. By contrast, if 2D R_1-RAS is executed with the additional l_1 norm, the rate distributions associated with each pattern are clearly identifiable (Fig. 4b). The low-frequency signal is also isolated and can be attributed to satellite transition (ST) signal. The CT powder patterns can be extracted from each rate distribution, revealing the patterns for glycine HCl and histidine HCl (Fig. 4c); however, the powder patterns are distorted, and the narrow pattern corresponding to histidine HCl appears to have residual signal from glycine HCl (*i.e.*, the broader, low-intensity features). 2D R_2-RAS cannot separate the patterns, since the R_2 distributions between the two samples are overlapped, mainly due to the large R_2 distribution from glycine HCl (Fig. S6, ESI‡).

3D RAS was used to process this entire 3D NMR dataset, initially without regularization. The resulting R_1–R_2 correlation map shows many artifacts and spurious signals with evidence of potentially three components in the mixture, which likely originate from the two R_1 terms for glycine HCl and a single R_1 and R_2 for histidine HCl (Fig. 4d). Processing the data with regularization, including a relatively large l_1 constraint (λ), reduces the R_1–R_2 correlation map to two distinct regions of signal (Fig. 4e). The optimal λ was first determined with a S-curve routine (Fig. S5, ESI‡), and then refined empirically (Fig. S4, ESI‡) by running 3D RAS with three different λ's until an optimal pattern separation was obtained with $\lambda = 50$. PCA denoising was not necessary for this dataset. In this case, only the frequency points that were associated with substantial regions of NMR signal intensity were used as input for eqn 11 (*i.e.* only the frequency points from *ca.* −100 to +70 kHz in this case) to reduce computational costs. These compounds have unique R_1's, but glycine HCl has a distribution of R_2 values, which overlaps with the small R_2 distribution of histidine HCl. Still, projecting the frequency dimension from suitable (R_1, R_2) regions reveals patterns that match exceptionally well with the ideal simulations for either species[58,59] (Fig. 4f). Regardless of the R_2 overlap, the additional information provided by the

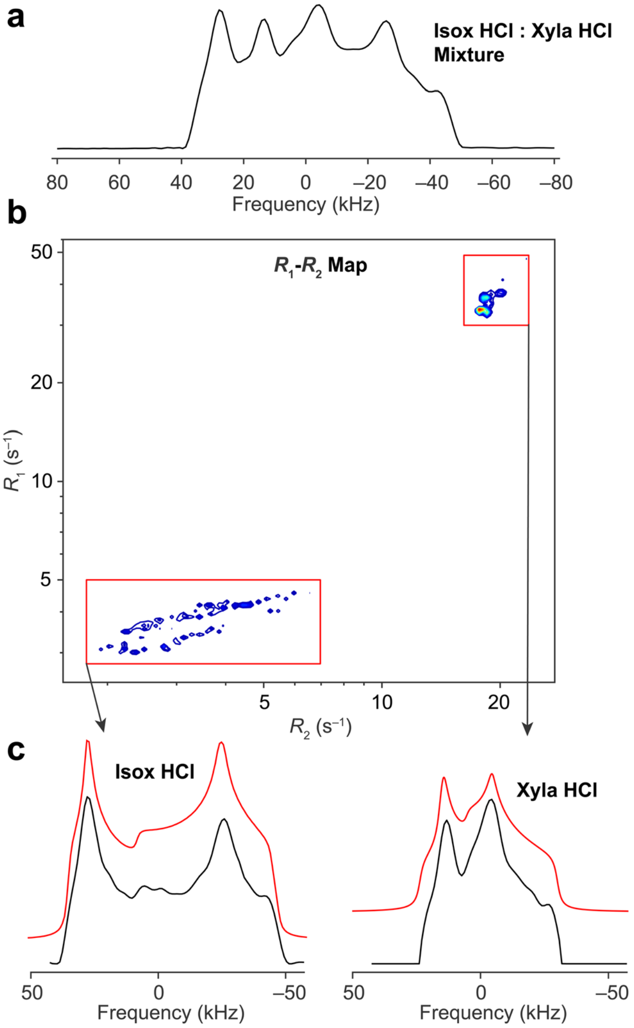

Fig. 5 (a) Experimental 1D ^{35}Cl NMR spectrum of an isoxsuprine (isox) HCl : xylazine (xyla) HCl 1 : 1 w/w mixture. (b) R_1–R_2 correlation map obtained from 3D RAS with sparse NNTF and PCA denoising with α = 0.0001 and λ = 5. PCA increased the SNR of the input data from 118 to 694. (c) Projections of the powder patterns from each rate distribution with ideal ^{35}Cl NMR simulations of each pattern in red.

R_2-dimension offers a higher-resolution separation of the powder patterns with 3D RAS than 2D RAS.

^{35}Cl NMR of an isoxsuprine HCl : xylazine HCl 1 : 1 w/w mixture was acquired with the direct excitation WCPMG-IR pulse sequence (Fig. 5a). An R_1–R_2 correlation map was obtained with 3D RAS using all of the aforementioned regularization methods as well as PCA denoising with three principal components (Fig. 5b); in this case, the SNR of the input data increases *ca.* 6-fold with PCA. This mixture serves as good test case, since the resulting R_1 and R_2 distributions are unique for both sites; the separation of the two patterns is very clear, and their projections match extremely well with the ideal simulated ^{35}Cl power patterns (Fig. 5c).[74]

3D RAS processing of a ^{35}Cl NMR dataset was also used for the characterization of a novel RbCl:CdCl$_2$:Urea cocrystal

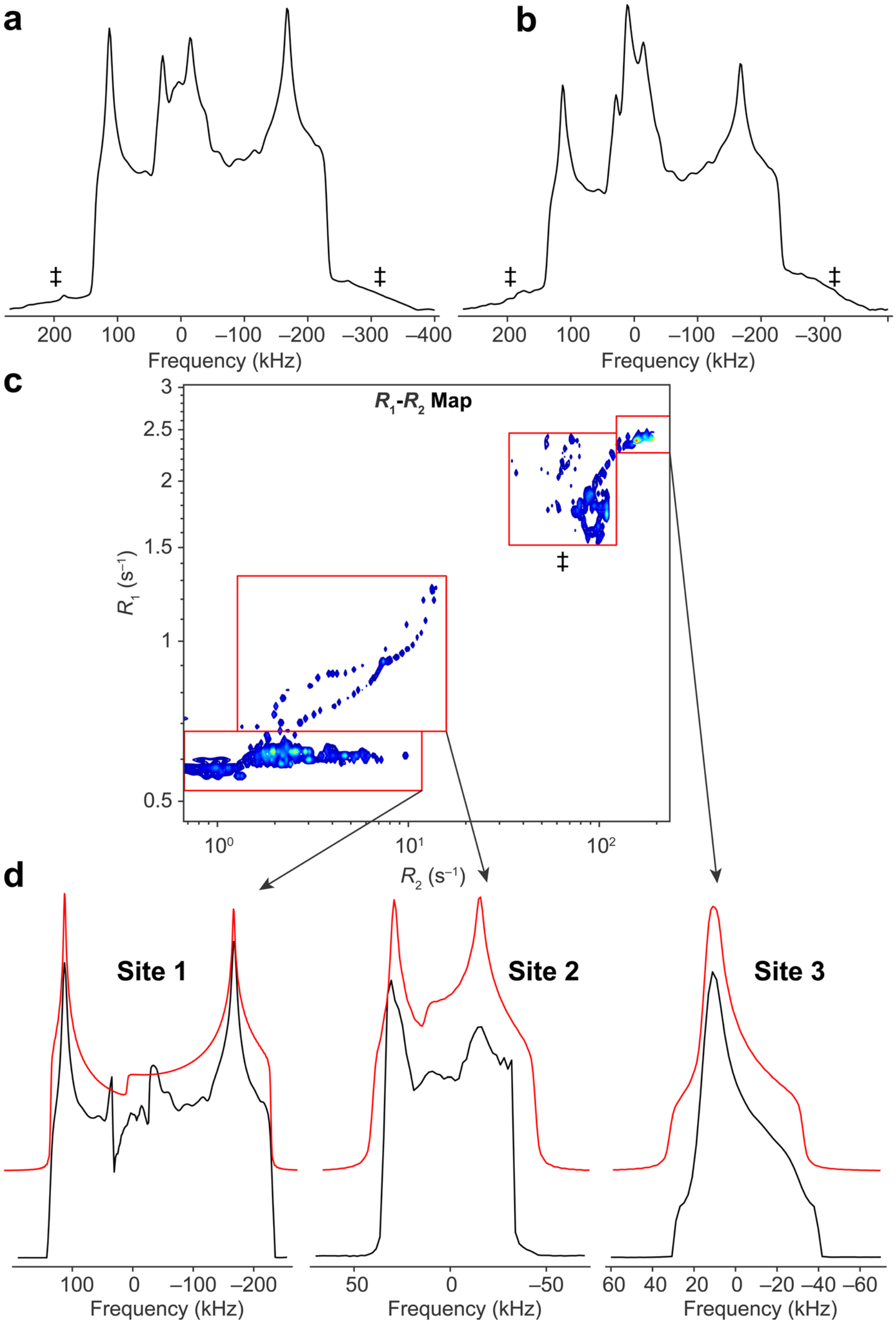

Fig. 6 (a) Experimental 1D ^{35}Cl NMR spectrum of a RbCl:CdCl$_2$:Urea cocrystal acquired with WCPMG and processed by coadding all 200 spin echoes and (b) processed by coadding the first 10 spin echoes. ‡ Indicates a broad powder pattern in (a and b) of unknown origin (*i.e.*, it is not clear if it is a unique CT pattern or signal arising from overlapping ST patterns). (c) R_1–R_2 correlation map obtained from 3D RAS with sparse NNTF and PCA denoising with α = 0.0001 and λ = 1. PCA increased the SNR of the data from 112 to 1450. The area between R_1 = 1.5 to 2.5 s^{-1} marked with ‡ corresponds to the unassigned broad pattern. (d) Projections of the CT powder patterns from each rate distribution with ^{35}Cl NMR simulations of each pattern in red.

synthesized by our research group. This material was first examined using 1D WCPMG, where two distinct CT powder patterns are observable, distinct from the $CdCl_2$ starting material (Fig. 6a and Fig. S7, ESI‡). A separate narrow resonance, which may be unreacted RbCl, is observable if fewer echoes from the CPMG train are processed (Fig. 6b). Additional signal above *ca.* 150 kHz and below *ca.* −230 kHz (as indicated by ‡) spans several hundreds of kHz and extends well beyond the tuning range of the probe – it cannot be assigned as another CT pattern or as ST patterns (Fig. S8, ESI‡); therefore, experimental acquisitions for RAS selectively and uniformly swept over only the ±350 kHz offset range. The R_1–R_2 correlation map displays the reconstructed signals that spread over several rate distributions (Fig. 6c). Projections from the lower R_1–R_2 distributions reveal separation of two of the CT powder patterns, possessing low η_Q's, and some residual overlap between them at *ca.* +40 and −50 kHz (Fig. 6d). There is also a distinctive high-valued R_1–R_2 distribution that reveals a narrow pattern with a higher value of η_Q that does not match with the NMR of bulk RbCl (Fig. 6d and Fig. S9, ESI‡) and likely corresponds to a novel site in the cocrystal. The separation of this latter pattern using 3D RAS can allow for the measurement of the EFG tensor parameters (Table S6, ESI‡), which would not be possible using standard 1D static or MAS NMR for this sample. Finally, the unassigned broad underlying pattern also has a distinct rate distribution, as indicated by ‡ (Fig. 6c).

3D RAS was also implemented for the separation of overlapping ^{2}H patterns of 1,8-dimethylnaphthalene-d_{12} (Fig. 7a), in which each ^{2}H site has a unique R_1 (*vide supra*) but overlapping distributions of R_2's. The sparse NNTF R_1–R_2 correlation map (Fig. 7b) shows two distinct regions of signal corresponding to each ^{2}H site. As discussed for the 2D R_1 RAS of this data, the R_1's are unique for each site, but both display a distribution over the R_1 dimension, which may be characteristic of R_1-anisotropy that has been widely observed for static ^{2}H NMR.[35,72,73] The R_2's clearly overlap for these sites, limiting the potential of 2D R_2 RAS for pattern separation; as in the case of ^{35}Cl NMR of glycine HCl, there is also a large distribution over the R_2 dimension for the ^{2}H-methyl site. Each static ^{2}H powder pattern can be resolved (Fig. 7c) with minor distortions in the case of the broad aromatic ^{2}H site (around ±20–50 kHz), likely from small residual spectral intensities arising from the much more intense methyl pattern.

A final example of 3D RAS's ability to resolve overlapping powder patterns is demonstrated for a ^{14}N NMR dataset of a glycine HCl : betaine HCl 1 : 1 w/w mixture. ^{14}N experiments yield UWNMR patterns that are very time-consuming to acquire;[75] however, it has been demonstrated that the combination of ^{1}H-^{14}N BRAIN-CP and targeted acquisitions with selected transmitter frequencies can accelerate this process.[76,77] Moreover, it has been demonstrated that spectral regions from only one half of the spin-1 ^{14}N patterns, are necessary for characterizing the EFG tensor parameters;[35,76,77] targeting one half of the integer-spin powder pattern also offers additional signal enhancement due to the direct enhancement of integer spin magnetization (DEISM) effect.[78] Experiments were accelerated by acquiring only half of the patterns;[79,80] in the current example, by sweeping all WURST pulses from low-to-high frequency. The 1D ^{14}N spectrum of the mixture was acquired with a targeted transmitter frequency such that the positive half of the betaine HCl pattern appears uniform, and the "horn" and shoulder" discontinuities of the glycine HCl pattern are visible (Fig. 8a); for the latter, these two discontinuities alone are sufficient to characterize the EFG tensor parameters.[76] 3D RAS data for the mixture were acquired with BRAIN-CP-IR; PCA denoising with 3 principal components was used, resulting in an increase in the SNR by a factor of *ca.* 10. The resulting regularized 3D RAS transformation reveals a R_1–R_2 correlation map showing two distinct R_1's, and partially overlapped R_2 distributions (Fig. 8b). As in the case of the ^{35}Cl glycine HCl:histidine HCl mixture (*cf.* Fig. 4), although the R_2 distributions are slightly overlapped, the added information from the R_2 dimension assists in the overall separation. The projections from these rate distributions show clearly resolved powder patterns that match well with simulations (Fig. 8c). The dip in the glycine

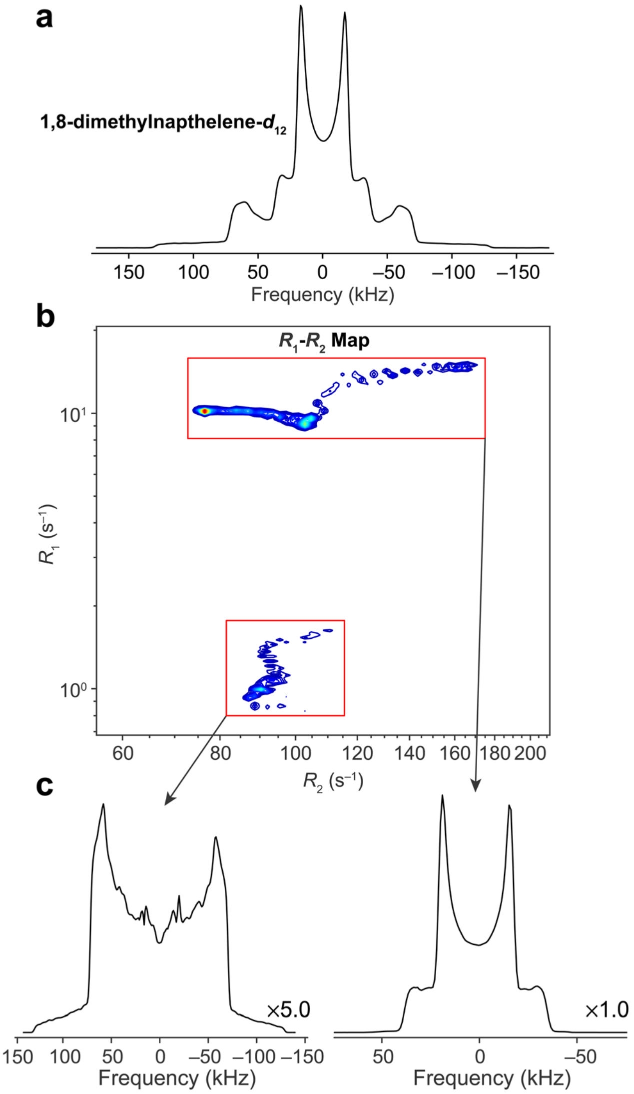

Fig. 7 (a) An experimental 1D ^{2}H NMR spectrum of 1,8-dimethylnapthalene-d_{12}. (b) R_1–R_2 correlation map obtained from 3D RAS with sparse NNTF with α = 0.001 and λ = 0.1. PCA denoising was not necessary for this dataset. (c) Projections of the powder patterns from each rate distribution.

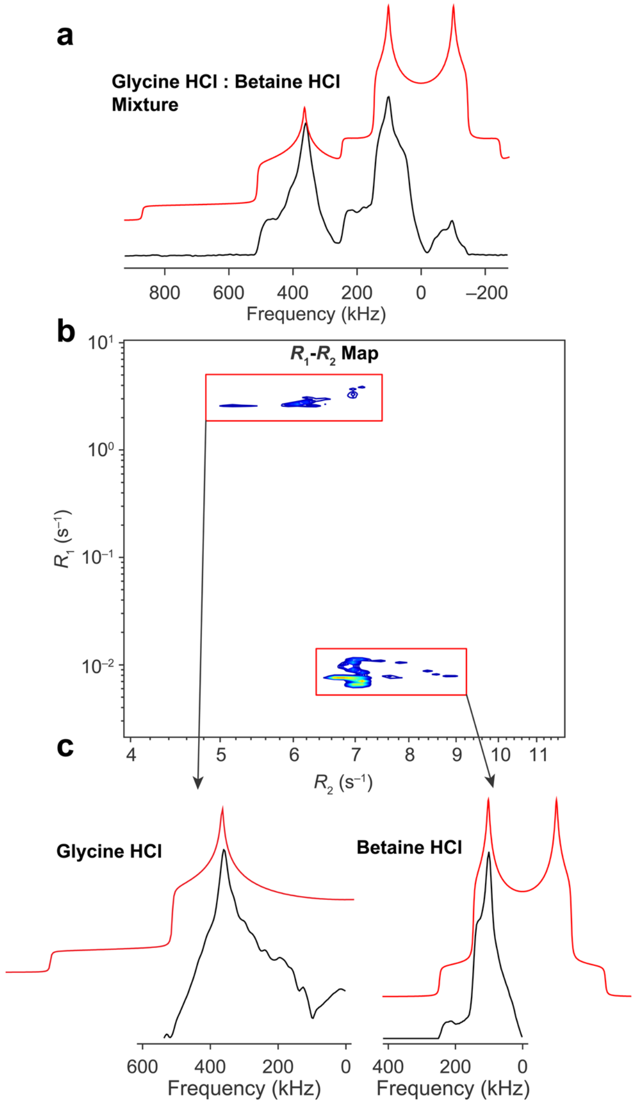

Fig. 8 (a) Experimental 1D ^{14}N NMR spectrum of a glycine HCl : betaine HCl 1 : 1 w/w mixture with a simulated ^{14}N spectrum of both ideal patterns summed together in red. (b) R_1–R_2 correlation map obtained from 3D RAS with sparse NNTF and PCA denoising with α = 0.0001 and λ = 0.0. PCA increased the SNR of the input data from 94 to 920. (c) Projections of the powder patterns from each rate distribution with ideal ^{14}N NMR simulations of each pattern in red. All WURST-A and WURST-B pulses in the sequence are swept from low-to-high frequency and the center offset of the sweep is set to +139 kHz with respect to ν_0(^{14}N).

HCl spectrum at *ca.* 100 kHz is characteristic of targeted spin-1 BRAIN-CP and is of no consequence for characterizing the powder pattern.[77,80] In this case, as well as all others, 3D RAS is only evaluated for frequency points associated with NMR signal in order to save on computation costs (*ca.* 0 to 550 kHz region).

5. Conclusions

2D and 3D RAS implemented with TSVD, EN regularization, and PCA denoising can provide clear separation of overlapping static UWNMR spectra, as demonstrated by experimentally acquired and numerically simulated ^{2}H (I = 1), ^{35}Cl (I = 3/2), and ^{14}N (I = 1) SSNMR spectra. TSVD greatly reduces computational costs for 2D and 3D RAS and regularizes sparse NNTF solutions. EN regularization further stabilizes these solutions, and in particular, the l_1-norm constraint can aid in the separation of powder patterns for samples with nuclei influenced by either multiexponential relaxation rates or distributions of rates. The SNR of the raw input data prior to RAS can be increased by up to 12-fold with PCA reconstruction. RAS is ultimately limited by experimental noise, requiring that the relaxation time constants associated with different nuclear sites and their concomitant powder patterns be unique from one another. Denoising and regularization schemes greatly alleviate these drawbacks, making RAS amenable to a wider array of possible samples, potentially even those with complex relaxation behaviour. The samples investigated herein are highly crystalline and their NMR data correspond to relatively sparse distributions of relaxation rates. We anticipate that further considerations and methodology will be required when analyzing amorphous samples that often yield broad distributions of relaxation rates (*e.g.*, alternative regression algorithms or the use of neural networks).[43,81] Even if non-equivalent sites do not have unique T_1's and/or (effective) T_2's, the rotating frame T_1, $T_{1\rho}$, and the dipolar frame T_1, T_{1D}, are also suitable exponential decay constants,[23,82] that could be encoded and used with the RAS processing described herein. Furthermore, if the effective T_2's of two magnetically distinct sites at a given decoupling power are similar, it may be possible to differentiate them further by varying the heteronuclear dipolar decoupling RF fields;[60] variation in CP efficiency with variable contact times could serve to highlight similar site differences.[83]

3D RAS is particularly useful for separating overlapping half-integer spin CT powder patterns of quadrupolar nuclei with large C_Q's, of the kind that cannot be resolved with MQMAS or STMAS. The example of a histidine HCl:glycine HCl mixture demonstrates the improved site resolution capabilities of 3D RAS over 2D RAS. The case of the isoxuprine HCl:xylazine HCl mixture suggests that RAS may be useful in the characterization of active pharmaceutical ingredients with ^{35}Cl NMR.[59,74] ^{2}H RAS of 1,8-dimethylnapthalene-d_{12} and ^{35}Cl RAS of RbCl:CdCl$_2$:Urea demonstrate the capabilities of site-resolution for multiple sites in the same sample – including in the latter example, the identification of a ^{35}Cl pattern and corresponding site that would not resolvable using other methodologies. WCPMG-IR, BRAIN-CP-IR, and QCPMG-IR pulse sequences used for RAS are facile to implement and the RAS routines have been written in end-user friendly functions in MATLAB that are freely available to use. It is anticipated that the aforementioned 2D and 3D RAS protocols will be used for high-resolution static and MAS SSNMR in a wide variety of organic, inorganic, organometallic, and hybrid systems with spin-1/2 and quadrupolar nuclei of elements across the Periodic Table.

Author contributions

M. J. J. and A. R. A. wrote the MATLAB code for RAS. A. R. A. acquired and processed the experimental datasets. All authors contributed to the writing of the manuscript.

Conflicts of interest

There are no conflicts to declare.

Acknowledgements

Cameron Vojvodin is thanked for synthesizing the RbCl:CdCl$_2$: Urea cocrystal. R. W. S. and A. R. A. would like to thank the National Science Foundation Chemical Measurement and Imaging Program, with partial co-funding from the Solid State and Materials Chemistry Program (NSF-2003854), for supporting this work, as well as The Florida State University and the National High Magnetic Field Laboratory (NHMFL), which is funded by the National Science Foundation Cooperative Agreement (DMR-1644779) and by the State of Florida. M. J. J. would like to thank the Perlman Family Foundation for a student-initiated research grant and the EU Horizon 2020 program (Marie Sklodowska-Curie Grant 642773). L. F. thanks the Israel Science Foundation (Grants 965/18); he holds the Bertha and Isadore Gudelsky Professorial Chair and Heads the Clore Institute for High-Field Magnetic Resonance Imaging and Spectroscopy at the Weizmann Institute, whose support is also acknowledged.

References

1 W. T. Dixon, *J. Chem. Phys.*, 1982, **77**, 1800–1809.
2 A. Bax, N. M. Szeverenyi and G. E. Maciel, *J. Magn. Reson.*, 1983, **52**, 147–152.
3 Z. Gan, *J. Am. Chem. Soc.*, 1992, **114**, 8307–8309.
4 L. Frydman and J. S. Harwood, *J. Am. Chem. Soc.*, 1995, **117**, 5367–5368.
5 A. Medek, J. S. Harwood and L. Frydman, *J. Am. Chem. Soc.*, 1995, **117**, 12779–12787.
6 Z. Gan, *J. Am. Chem. Soc.*, 2000, **122**, 3242–3243.
7 A. Samoson, E. Lippmaa and A. Pines, *Mol. Phys.*, 1988, **65**, 1013–1018.
8 Y. Wu, B. Sun, A. Pines, A. Samoson and E. Lippmaa, *J. Magn. Reson.*, 1990, **89**, 297–309.
9 A. Venkatesh, M. P. Hanrahan and A. J. Rossini, *Solid State Nucl. Magn. Reson.*, 2017, **84**, 171–181.
10 A. Venkatesh, X. Luan, F. A. Perras, I. Hung, W. Huang and A. J. Rossini, *Phys. Chem. Chem. Phys.*, 2020, **22**, 20815–20828.
11 I. Hung and Z. Gan, *J. Magn. Reson.*, 2021, **324**, 106913.
12 I. Hung and Z. Gan, *J. Magn. Reson.*, 2021, **328**, 106994.
13 Z. Gan, *J. Chem. Phys.*, 2001, **114**, 10845–10853.
14 H. J. Jakobsen, A. R. Hove, R. G. Hazell, H. Bildsøe and J. Skibsted, *Magn. Reson. Chem.*, 2006, **44**, 348–356.
15 H. J. Jakobsen, A. R. Hove, H. Bildsøe, J. Skibsted and M. Brorson, *J. Magn. Reson.*, 2007, **185**, 159–163.
16 T. Giavani, H. Bildsøe, J. Skibsted and H. J. Jakobsen, *J. Magn. Reson.*, 2004, **166**, 262–272.
17 J. H. Lee, C. Labadie, C. S. Springer, G. S. Harbison, J. H. Lee, C. Labadie, C. S. Springer and G. S. Harbison, *J. Am. Chem. Soc.*, 1993, **115**, 7761–7764.
18 P. Galvosas and P. T. Callaghan, *C. R. Phys.*, 2010, **11**, 172–180.
19 P. Berman, O. Levi, Y. Parmet, M. Saunders and Z. Wiesman, *Concepts Magn. Reson., Part A*, 2013, **42**, 72–88.
20 M. A. Bernstein, K. F. King and X. J. Zhou, *Handbook of MRI Pulse Sequences*, Elsevier, 2004.
21 Y.-Q. Song, *J. Magn. Reson.*, 2013, **229**, 12–24.
22 D. Topgaard, *J. Magn. Reson.*, 2017, **275**, 98–113.
23 A. Lupulescu, M. Kotecha and L. Frydman, *J. Am. Chem. Soc.*, 2003, **125**, 3376–3383.
24 T. Iijima and T. Shimizu, *Solid State Nucl. Magn. Reson.*, 2018, **91**, 1–8.
25 G. S. Boutis and R. Kausik, *Int. J. Mol. Sci.*, 2019, **20**, 5888.
26 M. J. Jaroszewicz, L. Frydman and R. W. Schurko, *J. Phys. Chem. A*, 2017, **121**, 51–65.
27 R. W. Schurko, *Acc. Chem. Res.*, 2013, **46**, 1985–1995.
28 E. Kupče and R. Freeman, *J. Magn. Reson., Ser. A*, 1995, **115**, 273–276.
29 E. Kupče and R. Freeman, *J. Magn. Reson., Ser. A*, 1995, **117**, 246–256.
30 L. A. O'Dell and R. W. Schurko, *Chem. Phys. Lett.*, 2008, **464**, 97–102.
31 K. J. Harris, A. Lupulescu, B. E. G. Lucier, L. Frydman and R. W. Schurko, *J. Magn. Reson.*, 2012, **224**, 38–47.
32 J. S. Frye, *Concepts Magn. Reson.*, 1989, **1**, 27–33.
33 H. Y. Carr and E. M. Purcell, *Phys. Rev.*, 1954, **94**, 630–638.
34 S. Meiboom and D. Gill, *Rev. Sci. Instrum.*, 1958, **29**, 688–691.
35 A. R. Altenhof, M. J. Jaroszewicz, K. J. Harris and R. W. Schurko, *J. Chem. Phys.*, 2021, **154**, 034202.
36 L. A. O'Dell, *Solid State Nucl. Magn. Reson.*, 2013, **55–56**, 28–41.
37 R. W. Schurko, *Encyclopedia of Magnetic Resonance*, John Wiley & Sons, Ltd, Chichester, UK, 2011, pp. 77–93.
38 J. Mitchell, T. C. Chandrasekera and L. F. Gladden, *Prog. Nucl. Magn. Reson. Spectrosc.*, 2012, **62**, 34–50.
39 A. N. Tikhonov and V. Arsenin, *Solutions of Ill Posed Problems*, Wiley, New York, 1977.
40 C. W. Groetsch, *The Theory of Tikhonov Regularization for Fredholm Equations of the First Kind*, Pitman Publishing, Boston, 1984.
41 L. Venkataramanan, Y. Q. Song and M. D. Hürlimann, *IEEE Trans. Signal Process.*, 2002, **50**, 1017–1026.
42 Y.-Q. Song, L. Venkataramanan, M. D. Hürlimann, M. Flaum, P. Frulla and C. Straley, *J. Magn. Reson.*, 2002, **154**, 261–268.
43 D. J. Srivastava and P. J. Grandinetti, *J. Chem. Phys.*, 2020, **153**, 134201.
44 J. Guo, R. Xie, L. Xiao, G. Jin and L. Gao, *J. Magn. Reson.*, 2019, **308**, 106562.
45 S.-J. Kim, K. Koh, M. Lustig, S. Boyd and D. Gorinevsky, *IEEE J. Sel. Top. Signal Process.*, 2007, **1**, 606–617.
46 P. D. Teal and E. H. Novotny, *J. Magn. Reson.*, 2021, 107124.
47 C. Sabett, A. Hafftka, K. Sexton and R. G. Spencer, *Concepts Magn. Reson., Part A*, 2017, **46A**, e21427.
48 T. Parasram, R. Daoud and D. Xiao, *J. Magn. Reson.*, 2021, **325**, 106930.
49 Y. Kusaka, T. Hasegawa and H. Kaji, *J. Phys. Chem. A*, 2019, **123**, 10333–10338.

50 O. V. Petrov, J. Lang and M. Vogel, *J. Magn. Reson.*, 2021, **326**, 106965.

51 D. Kim, J. L. Wisnowski, C. T. Nguyen and J. P. Haldar, *NMR Biomed.*, 2020, 1–19.

52 R. Enjilela, J. Guo, B. MacMillan, F. Marica, A. Afrough and B. Balcom, *J. Magn. Reson.*, 2021, 106961.

53 M. V. Afonso, J. M. Bioucas-Dias and M. A. T. Figueiredo, *IEEE Trans. Image Process.*, 2011, **20**, 681–695.

54 P. C. Hansen, *Inverse Probl.*, 1992, **8**, 849–872.

55 P. C. Hansen, *Numer. Algorithms*, 1994, **6**, 1–35.

56 J. Guo, B. Macmillan, S. Zamiri and B. Balcom, *J. Magn. Reson.*, 2021, 107005.

57 R. Varshavsky, A. Gottlieb, M. Linial and D. Horn, *Bioinformatics*, 2006, **22**, e507–e513.

58 D. L. Bryce, G. D. Sward and S. Adiga, *J. Am. Chem. Soc.*, 2006, **128**, 2121–2134.

59 D. A. Hirsh, A. J. Rossini, L. Emsley and R. W. Schurko, *Phys. Chem. Chem. Phys.*, 2016, **18**, 25893–25904.

60 S. L. Veinberg, Z. W. Friedl, K. J. Harris, L. A. O'Dell and R. W. Schurko, *CrystEngComm*, 2015, **17**, 5225–5236.

61 Z. Gan, P. Robyr and R. R. Ernst, *Chem. Phys. Lett.*, 1998, **283**, 262–268.

62 A. R. Altenhof, M. J. Jaroszewicz, A. W. Lindquist, L. D. D. Foster, S. L. Veinberg and R. W. Schurko, *J. Phys. Chem. C*, 2020, **124**, 14730–14744.

63 G. Laurent, W. Woelffel, V. Barret-Vivin, E. Gouillart and C. Bonhomme, *Appl. Spectrosc. Rev.*, 2019, **54**, 602–630.

64 S. G. Hyberts, S. A. Robson and G. Wagner, *J. Biomol. NMR*, 2013, **55**, 167–178.

65 T. Iijima and K. Nishimura, *Chem. Phys. Lett.*, 2011, **514**, 181–186.

66 T. Iijima, T. Shimizu and K. Nishimura, *J. Magn. Reson.*, 2015, **251**, 57–64.

67 A. R. Altenhof, Z. Gan and R. W. Schurko, *J. Magn. Reson.*, 2022, **337**, 107174.

68 E. D. Ostroff and J. S. Waugh, *Phys. Rev. Lett.*, 1966, **16**, 1097–1098.

69 P. Mansfield and D. Ware, *Phys. Lett.*, 1966, **22**, 133–135.

70 J. S. Waugh and C. H. Wang, *Phys. Rev.*, 1967, **162**, 209–216.

71 W.-K. Rhim, D. P. Burum and D. D. Elleman, *Phys. Rev. Lett.*, 1976, **37**, 1764–1766.

72 R. J. Wittebort, E. T. Olejniczaka and R. G. Griffin, *J. Chem. Phys.*, 1987, **86**, 5411–5420.

73 J. R. Long, R. Ebelhäuser and R. G. Griffin, *J. Phys. Chem. A*, 1997, **101**, 988–994.

74 A. M. Namespetra, D. A. Hirsh, M. P. Hildebrand, A. R. Sandre, H. Hamaed, J. M. Rawson and R. W. Schurko, *CrystEngComm*, 2016, **18**, 6213–6232.

75 L. A. O'Dell, *Prog. Nucl. Magn. Reson. Spectrosc.*, 2011, **59**, 295–318.

76 S. L. Veinberg, A. W. Lindquist, M. J. Jaroszewicz and R. W. Schurko, *Solid State Nucl. Magn. Reson.*, 2016, 1–14.

77 K. J. Harris, S. L. Veinberg, C. R. Mireault, A. Lupulescu, L. Frydman and R. W. Schurko, *Chem. – Eur. J.*, 2013, **19**, 16469–16475.

78 L. A. O'Dell and R. W. Schurko, *J. Am. Chem. Soc.*, 2009, **131**, 6658–6659.

79 J. Koppe and M. R. Hansen, *J. Phys. Chem. A*, 2020, **124**, 4314–4321.

80 A. R. Altenhof, S. Wi and R. W. Schurko, *Magn. Reson. Chem.*, 2021, **59**, 1009–1023.

81 S. G. Worswick, J. A. Spencer, G. Jeschke and I. Kuprov, *Sci. Adv.*, 2018, **4**, eaat5218.

82 K. Akasaka, S. Ganapathy, C. A. McDowell and A. Naito, *J. Chem. Phys.*, 1983, **78**, 3567–3572.

83 H. E. Mason, E. C. Uribe and J. A. Shusterman, *Phys. Chem. Chem. Phys.*, 2018, **20**, 18082–18088.